Calibration of Non-SVP Hyperbolic Catadioptric Robotic Vision Systems

Bernardo Cunha, José Azevedo and Nuno Lau
ATRI-IEETA/DETI, Universidade de Aveiro
Portugal

1. Introduction

RoboCup (http://www.robocup.org) is an international worldwide initiative that aims to promote research and development in mobile robotics and related areas. Robotic soccer is one of the proposed problems since it represents a challenge of high complexity, in which fully autonomous robots cooperate in order to achieve a common goal (win the game). Within Robocup soccer competitions, the Middle-Size League proposes a challenge where two teams of five fast robots, measuring up to 80cm and weighting up to 40Kg, play soccer in a 18x12m field in a semi-structured, highly dynamic environment. This challenge requires a real time perception of the overall environment in order to allow self localization, mate and opponent localization and, of course, determination of the ball position and movement vector. This, in practice, determines that adopting an omni-directional vision system, as the main sensorial element of the robot, although not mandatory, has significant advantages over other solutions such as standard panoramic vision systems. A common solution found in robots from most teams of this competition, as well as in robots for other autonomous mobile robot applications, is based on a catadioptric omni-directional vision system composed of a regular video camera pointed at a hyperbolic mirror – or any other mirror obtained from a solid of revolution (e.g. ellipsoidal convex mirror). This is the case, just to name a few, of those teams described in (Zivkovic & Booij, 2006), (Wolf, 2003), (Menegatti et al, 2001, 2004) and (Lima et al, 2001).

This type of setup ensures an integrated perception of all major target objects in the robots surrounding area, allowing a higher degree of maneuverability at the cost of higher resolution degradation with growing distances away from the robot (Baker & Nayar, 1999) when compared to non-isotropic setups. For most practical applications, as is the case of the RoboCup competition, this setup requires the translation of the planar field of view, at the camera sensor plane, into real world coordinates at the ground plane, using the robot as the center of this system. In order to simplify this non-linear transformation, most practical solutions adopted in real robots choose to create a mechanical geometric setup that ensures a symmetrical solution for the problem by means of single viewpoint (SVP) approach (Zivkovic & Booij, 2006), (Wolf, 2003) and (Lima et al, 2001). This, on the other hand, calls for a precise alignment of the four major points comprising the vision setup: the mirror focus, the mirror apex, the lens focus and the center of the image sensor. Furthermore, it also

demands the sensor plane to be both parallel to the ground field and normal to the mirror axis of revolution, and the mirror foci to be coincident with the effective viewpoint and the camera pinhole (Benosman & Kang, 2001). Although tempting, this approach requires a precision mechanical setup and generally precludes the use of low cost video cameras, due to the commonly found problem of translational and angular misalignment between the image sensor and the lens plane and focus. In these cameras the lens is, most of the times, attached to a low stability plastic mechanical system that further adds to this problem. Furthermore, the game itself, where robots sometimes crash against each other, or where the ball can violently be shot against other robots (sometimes striking the vision sub-system), tends to mechanically misalign this system over time.

In this chapter we describe a general solution to calculate the robot centered distances map on non-SVP catadioptric setups, exploring a back-propagation ray-tracing approach and the mathematical properties of the mirror surface as explained by (Blinn,J.F. , 1977) and (Foley et al, 1995). This solution effectively compensates for the misalignments that may result either from a simple mechanical setup or from the use of low cost video cameras. Therefore, precise mechanical alignment and high quality cameras are no longer pre-requisites to obtain useful distance maps of the ground floor, reducing significantly the overall cost of the robot and providing a fast method for misalignment compensation over time.

The method described in this chapter can also extract most of the required parameters from the acquired image itself, allowing it to be used for self-calibration purposes. Results from this technique applied in the robots of the CAMBADA team (Cooperative Autonomous Mobile robots with Advanced Distributed Architecture) are presented, showing the effectiveness of the solution.

This first section of the chapter provides the introduction. Section 2 presents the related work on calibration of catadioptric vision systems, including both SVP and non-SVP setups. The next section describes the characteristics of the vision system used by the CAMBADA team. Section 4 discusses, in a constructive manner, the developed calibration methodologies. Two visual feedback tools that can be used to further trim the vision system parameters, in a semi-automated solution, are presented in section 5. Finally, section 6 concludes the chapter.

2. Related work

A significant amount of work exists referring to the development of methods for calibration of catadioptric camera systems. A very complete calibration method survey is presented by (Scaramussas, D., 2008), including auto-calibration by means of laser range finder and cross-matching between laser and camera images. However, most of the proposed calibration methods assume the single view point system. This is the case of (Kang, 2000) who proposed a self-calibration method for a catadioptric camera system that consists of a paraboloidal mirror and an orthographic lens by using the mirror boundary on the image. It assumes, however, that this boundary is a circle, restricting the possible mirror posture in the system. (Barreto and Araujo, 2002) also proposed a method for central catadioptric camera calibration based on lines as geometrical invariants. (Geyer and Daniilidis, 2002) proposed a method of calibration to estimate intrinsic parameters of a catadioptric camera system that consists of a paraboloidal mirror and an orthographic lens. These calibration methods, however, are only for para-catadioptric cameras, configurations which have a

unique effective viewpoint and in which the reflective surface is a parabolic mirror that, together with the camera, induces an orthographic projection. (Ying and Hu, 2003) proposed a central catadioptric camera calibration method that uses images of lines or images of spheres as geometric invariants. (Micusik and Pajdla, 2004) also proposed another method for para-catadioptric camera self calibration from point correspondences in two views based on the epipolar constraint. (Micusik, B. and Pajdla, T., 2006) present a calibration method based on matching points in different perspective images. Outliers are excluded by the use of RANSAC. Although this paper discusses the application to real world systems the presented solution is valid for SVP orthographic solutions only. As previously stated, all these methods are effective only for central catadioptric cameras, assuming the SVP restriction.

Less work has been done on calibration methods for non-SVP catadioptric cameras. (Aliaga, 2001) proposed a paracatadioptric camera calibration method which relaxes the assumption of the perfect orthographic placement and projection. (Stelow et al, 2001) proposed a model for the relation between the mirror and camera which integrates translation and rotation of the mirror. The accuracy of this method, while estimating parameters, depends on the initial values, due to nonlinear optimization, and produces poor results. (Micusik and Pajdla, 2004) also proposed an auto-calibration and 3D reconstruction method by using a mirror boundary and an epipolar geometry approach. In this method, they also assume that the mirror boundary in the image is a circle. These methods are effective while compensating for minor mirror misalignments. (Mashita et al, 2006) also proposed a calibration method for a catadioptric camera system that they claim can estimate all degrees of freedom of mirror posture. This method assumes five degrees of freedom for the mirror, and uses the mirror boundary to determine the elliptic pattern on the image. It also proposes a selection method for finding the best solution, since the method produces more than one. This approach does not, however, consider the effect of the non normal restriction between the mirror axes of revolution and the plane of reference of the robot (in our application, the floor). It also depends significantly on the image resolution and contrast (either in luminance or chrominance) for an effective and precise evaluation of the mirror elliptic pattern in the image. (Voigtländer et al, 2007) present a method using piecewise linear functions in polar coordinates. They determine 12 support vectors for 45 different directions based on a calibration pattern placed on the ground.

3. The framework

In the following discussion the specific vision setup used in the CAMBADA team of robots will be assumed (Fig. 1). This can be generalized for other configurations, including the use of different types of mirrors, as long as their surface can be described by an analytical expression.

The setup comprises a catadioptric vision module mounted on top of a mechanical structure, and lies between 60cm and 80cm above the ground. It includes a low cost Fire-I Point Grey FL2-08S2C video camera with a 4mm focal distance inexpensive lens. This camera uses a 1/3" CCD sensor providing a resolution of 1032x776 pixels. The camera is set to acquire images with a 640x480 pixel size, at an acquisition rate of 30 frames/second. The main characteristics of the sensor, including pixel size, can be depicted in Fig. 2.

The mirror, used in the CAMBADA robot setup, has a hyperbolic surface, described by the following equation:

$$\frac{y^2}{1000} - \frac{\left(x^2 + z^2\right)}{1000} = 1 \quad \text{(mm)} \ . \tag{1}$$

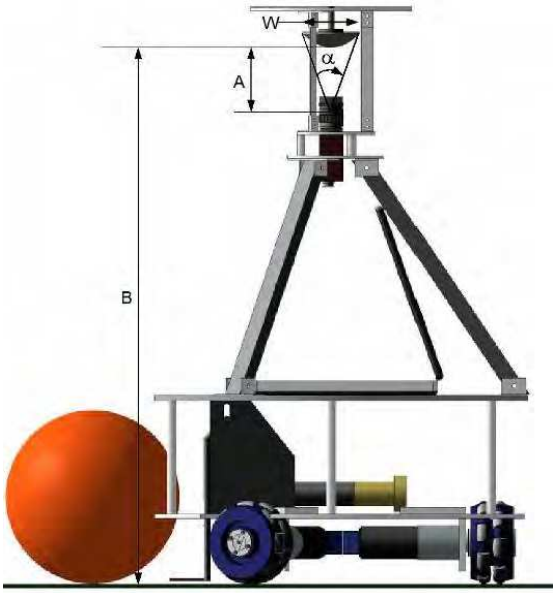

Fig. 1. The robot setup with the top catadioptric vision system.

where ***y*** is mirror axis of revolution and *z* is the axis parallel to a line that connects the robot center to its front. The mirror maximum radius is 35mm and the mirror depth, obtained from its equation, is 15.55mm. Height from the mirror apex to the ground plane is roughly 680mm, while distance from the mirror apex to the lens focus is approximately 110mm.

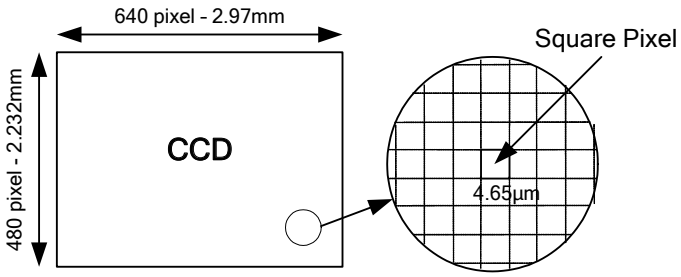

Fig. 2. The Point Grey camera CCD main characteristics, in 640x480 acquisition mode.

Some simplifications will also be used in regard with the diffraction part of the setup. The used lens has a narrow field of view and must be able to be focused at a short distance. This, together with the depth of the mirror, implies a reduced depth of field and therefore an associated defocus blur problem (Baker & Nayar, 1999). Fortunately, since spatial resolution of the acquired mirror image decreases significantly as distance to the seen object gets higher, this problem has a low impact in the solution when compared with the low-resolution problem itself. The focus plane is adjusted to be slightly behind the mirror apex so that objects in the vicinity of the robot are well defined, as this is the area where precise measurements, namely the distance to the ball, is actually relevant.
A narrow field of view, on the other hand, also reduces achromaticity aberration and radial distortion introduced by the lens. Camera/lenses calibration procedures are a well-known problem and are widely described in the literature (Zhang, 2000) and (Hartley & Zisserman, 2004). The setup has been tested with both 4mm and 6mm inexpensive lenses. The second requires a bigger distance between the camera and the mirror, increasing the overall volume of the catadioptric system. It also produces a narrower field of view when compared with the 4mm lens, reducing de radial distortion. The 4mm lens produces a more compact mechanical solution at the expense of greater radial distortion and smaller depth of field.
For compensating for radial distortion, a chess-board like black and white pattern is placed in front of the camera while removing the mirror (Fig. 3). The mirror support is used to place this pattern.

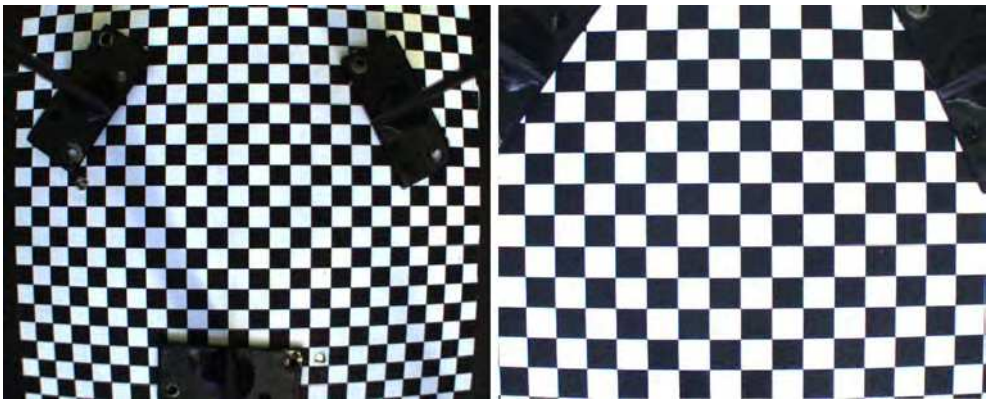

Fig. 3. The chess-board pattern seen by the Point Grey camera with a 4mm (left) and a 6mm (right) lenses respectively.

Automatic determination of pattern interception points in the image is followed by generation of the coefficients of a third order polynomial equation of the form

$$C(\theta) = k_0 + k_1\theta + k_2\theta^2 + k_3\theta^3 \ . \tag{2}$$

where $C(\theta)$ is the additive correction factor applied to the angle of any ray vector exiting the lens relative to the lens central plane (Fig. 4). The third order term is usually enough to model medium to large field of view lenses.
Coefficients are calculated using an iterative method that minimizes the co-variance of the two functions in the discrete domain.

The polynomial function is used both to determine the focal distance at the center of the image and to correct the diffraction angle produced by the lens. With the tested lenses the actual focal distance for the 4mm lens, obtained by this method, is 4.56mm while, for the 6mm lens, the actual focal distance is 6.77mm.
Polynomial coefficients K_0, K_1, K_2 and K_3, calculated for the two tested lenses, are respectively [0, 0, 0.001, .0045] and [0, 0, 0.0002, 0.00075].

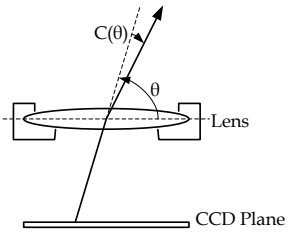

Fig. 4. Correction of radial distortion as a function of θ.

Using this method we will also assume that the pinhole model can provide an accurate enough approach for our practical setup, therefore disregarding any other distortion of the lens.

4.Discussion

Instead of elaborating on the general problem from the beginning, we will start by applying some restrictions to it that will simplify the initial solution. Later on, these restrictions will be relaxed in order to find a general solution.

4.1 Initial approach

Let's start by assuming a restricted setup as depicted in Fig. 5.
Assumptions applied to this setup are as follows:

- The origin of the coordinate system is coincident with the camera pinhole through which all light rays will pass;
- i, j and k are unit vectors along axis X, Y and Z, respectively;
- The Y axis is parallel to the mirror axis of revolution and normal to the ground plane;
- CCD major axis is parallel to the X system axis;
- CCD plane is parallel to the XZ plane;
- Mirror foci do not necessarily lie on the Y system axis;
- The vector that connects the robot center to its front is parallel and has the same direction as the positive system Z axis;
- Distances from the lens focus to the CCD plane and from the mirror apex to the XZ plane are htf and mtf respectively and can be readily available from the setup and from manufacturer data;
- Point $Pm(m_{cx}, 0, m_{cz})$ is the intersection point of the mirror axis of revolution with the XZ plane;
- Distance unit used throughout this discussion will be the millimeter.

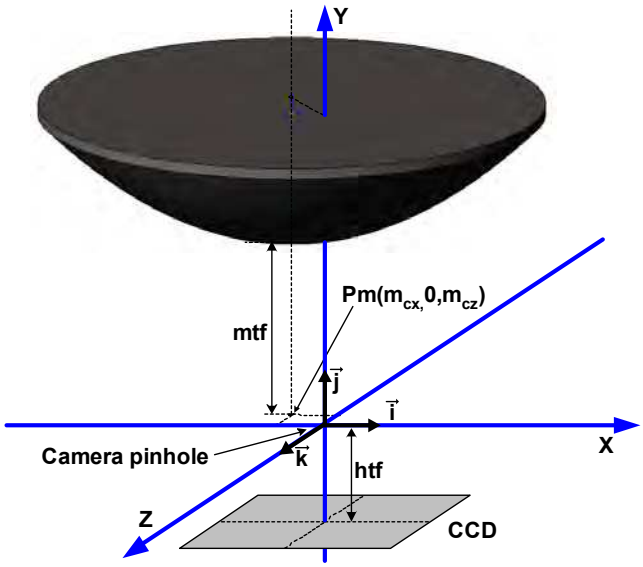

Fig. 5. The restricted setup with its coordinate system axis (***X, Y, Z***), mirror and CCD. The axis origin is coincident with the camera pinhole. Note: objects are not drawn to scale.

Given equation (1) and mapping it into the defined coordinate system, we can rewrite the mirror equation as

$$y = \sqrt{1000 + (x - m_{cx})^2 + (z - m_{cz})^2} + K_{off} \ . \tag{3}$$

where

$$k_{off} = mtf - \sqrt{1000} \ . \tag{4}$$

Let's now assume a randomly selected CCD pixel ($X_x X_z$), at point $Pp(p_{cx}, -htf, p_{cz})$, as shown in Fig. 6, knowing that

$$\frac{p_{cx}}{X_x} = \frac{p_{cz}}{X_z} = \frac{4.65 \times 10^{-3}}{1} \ . \tag{5}$$

The back propagation ray that starts at point $Pp(p_{cx}, -htf, p_{cz})$ and crosses the origin, after correction for the radial distortion, may or may not intersect the mirror surface. This can be easily evaluated from the ray vector equation, solving $P_i(x(y), y, z(y))$ for $y = mtf + md$, where ***md*** is the mirror depth. If the vector module $|P_b P_i|$ is greater than the mirror maximum radius then the ray will not intersect the mirror and the selected pixel will not contribute to the distance map.

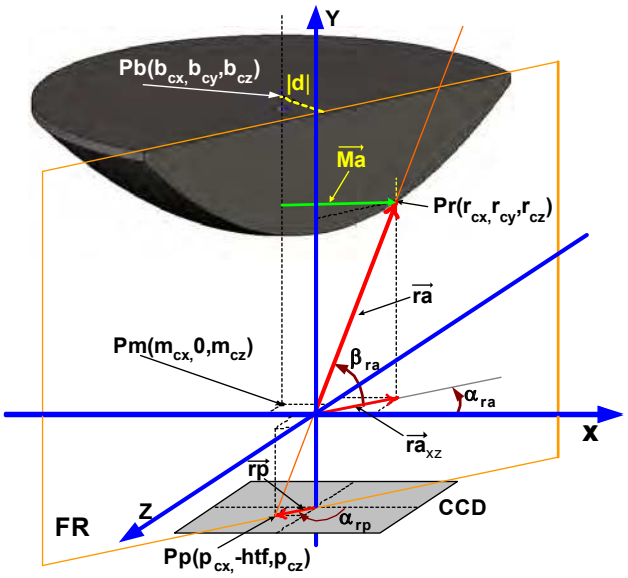

Fig. 6. A random pixel in the CCD sensor plane is the start point for the back propagation ray. This ray and the ***Y*** axis form a plane, ***FR***, that intersects vertically the mirror solid. ***Pr*** is the intersection point between ***ra*** and the mirror surface.

Assuming now that this particular ray will intersect the mirror surface, we can then come to the conclusion that the plane ***FR***, normal to ***XZ*** and containing this line, will cut the mirror parallel to its axis of revolution. This plane can be defined by equation

$$z = x\tan(\alpha_{ra}) \ . \tag{6}$$

The line containing position vector **ra,** assumed to lie on plane defined by eq. 6, can be expressed as a function of ***X*** as

$$y = x\tan(\beta_{ra})/\cos(\alpha_{ra}) \ . \tag{7}$$

where

$$\alpha_{ra} = \tan^{-1}\left(\frac{p_{cz}}{p_{cx}}\right) + pi \qquad \beta_{ra} = \tan^{-1}\left(\frac{htf}{\sqrt{p_{cx}^{\ 2} + p_{cz}^{\ 2}}}\right) . \tag{8}$$

Substituting (6) and (7) into (3) we get the equation of the line of intersection between the mirror surface and plane ***FR***, The intersection point, ***Pr***, which belong both to **ra** and to the mirror surface, can then be determined from the equality

$$\frac{x\tan(\beta_{ra})}{\cos(\alpha_{ra})} = \sqrt{1000 + (x - m_{cx})^2 + (x\tan(\alpha_{ra}) - m_{cz})^2} + K_{off} \ . \tag{9}$$

Equation (9) can, on the other hand, be transformed into a quadratic equation of the form

$$ax^2 + bx + c = 0 \tag{10}$$

where

$$a = \left(1 + {k_{tn}}^2 - {k_{tc}}^2\right). \tag{11}$$

$$b = 2\left(k_{tc}k_{off} - k_{tn}m_{cz} - m_{cx}\right). \tag{12}$$

$$c = 1000 + {m_{cz}}^2 + {m_{cx}}^2 - {K_{off}}^2. \tag{13}$$

and

$$k_{tc} = \frac{\tan(\beta_{ra})}{\cos(\alpha_{ra})} \qquad k_{tn} = \tan(\alpha_{ra}). \tag{14}$$

Assuming that we have already determined that there is a valid intersection point, this equation will have two solutions: one for the physical mirror surface, and other for the symmetrical virtual one. Given the current coordinate system, the one with the higher ***y*** value will correspond to the intersection point ***Pr***.

Having found ***Pr***, we can now consider the plane ***FN*** (Fig. 7) defined by ***Pr*** and by the mirror axis of revolution.

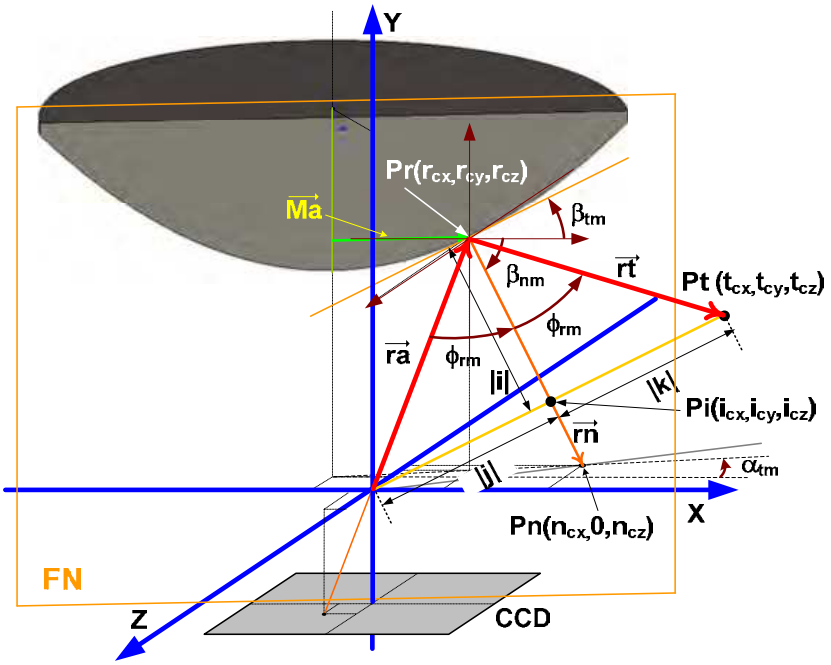

Fig. 7. Determining the normal to the mirror surface at point ***Pr*** and the equation for the reflected ray.

In this plane, we can obtain the angle of the normal to the mirror surface at point ***Pr*** by equating the derivative of the hyperbolic function at that point, as a function of ***|Ma|***

$$\frac{\partial h}{d\left|\overrightarrow{M_a}\right|} = \frac{\left|\overrightarrow{M_a}\right|}{\sqrt{1000 + \left|\overrightarrow{M_a}\right|^2}} \qquad \beta_{tm} = \tan^{-1}\left(\frac{\left|\overrightarrow{M_a}\right|}{\sqrt{1000 + \left|\overrightarrow{M_a}\right|^2}}\right) - \pi/2 \,. \tag{15}$$

This normal line intercepts the ***XZ*** plane at point ***Pn***

$$Pn = \left\{ r_{cx} - r_{cy}\frac{\cos(\alpha_{nm})}{\tan(\beta_{nm})}, 0, r_{cz} - r_{cy}\frac{\sin(\alpha_{nm})}{\tan(\beta_{nm})} \right\} \,. \tag{16}$$

where

$$\alpha_{nm} = \tan^{-1}\left(\frac{r_{cz} - m_{cz}}{r_{cx} - m_{cx}}\right) \,. \tag{17}$$

The angle between the incident ray and the normal at the incidence point can be obtained from the dot product between the two vectors, ***-ra*** and ***rn***. Solving for ϕ_{rm}:

$$\phi_{rm} = \cos^{-1}\left(\frac{r_{cx}(r_{cx} - n_{cx}) + r_{cy}(r_{cy} - n_{cy}) + r_{cz}(r_{cz} - n_{cz})}{\left|\overrightarrow{ra}\right|\left|\overrightarrow{rn}\right|}\right) \,. \tag{18}$$

The reflection ray vector, ***rt***, (Fig. 8) starts at point ***Pr*** and lies on a line going through point ***Pt*** where

$$Pt = \{t_{cx}, t_{cy}, t_{cz}\} = \{2i_{cx}, 2i_{cy}, 2i_{cz}\} \,. \tag{19}$$

$$\left|\overrightarrow{ri}\right| = \left|\overrightarrow{ra}\right|\cos(\phi_{rm}) \qquad \text{and} \qquad i_{cx} = r_{cx} + \left|\overrightarrow{ri}\right|\cos(\beta_{nm})\cos(\alpha_{nm}) \,. \tag{20}$$

$$i_{cy} = r_{cy} + \left|\overrightarrow{ri}\right|\sin(\beta_{nm}) \,. \tag{21}$$

$$i_{cz} = r_{cz} + \left|\overrightarrow{ri}\right|\cos(\beta_{nm})\sin(\alpha_{nm}) \,. \tag{22}$$

Its line equation will therefore be

$$P = (r_{cx}\vec{i} + r_{cy}\vec{j} + r_{cz}\vec{k}) + u((t_{cx} - r_{cx})\vec{i} + (t_{cy} - r_{cy})\vec{j} + (t_{cz} - r_{cz})\vec{k}) \,. \tag{23}$$

Note that if $(t_{cz}\text{-}r_{cz})$ is equal or greater than zero, the reflected ray will be above the horizon and will not intersect the ground. Otherwise, the point ***Pg*** can be obtained from the mirror to ground height ***hmf***, and from the ground plane and ***rt*** line equations (23), which, evaluating for ***u*** (23), gives

$$u = \frac{(mtf - hmf) - r_{cy}}{t_{cy} - r_{cy}} \tag{24}$$

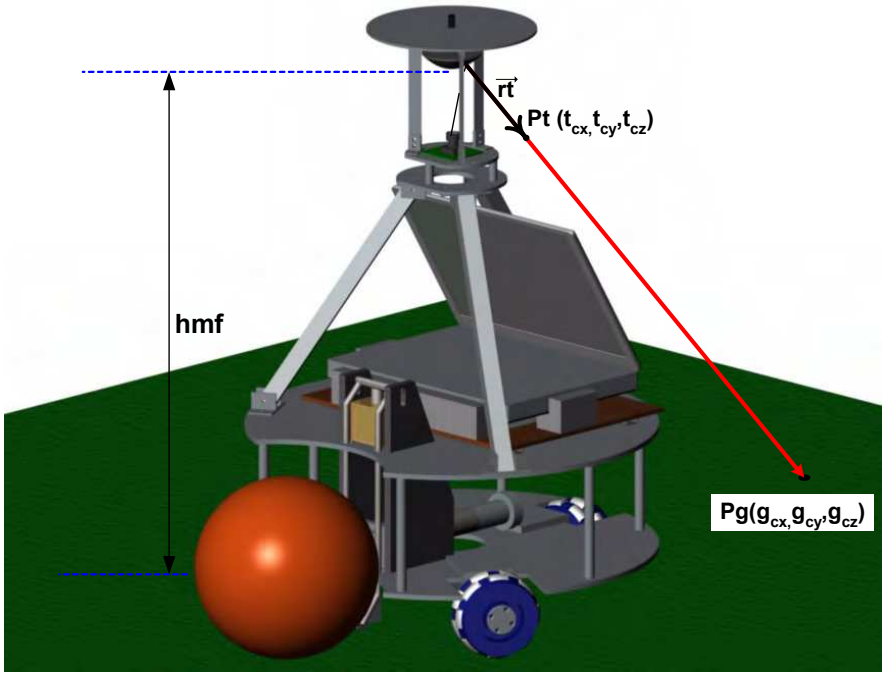

Fig. 8. (**Pg**) will be the point on the ground plane for the back-propagation ray.

4.2 Generalization

The previous discussion was constrained to a set of restrictions that would not normally be easy to comply to in a practical setup. In particular, the following misalignment factors would normally be found in a real robot using low cost cameras:

- The CCD plane may be not perfectly parallel to the ***XZ*** plane;
- The CCD minor axis may not be correctly aligned with the vector that connects the robot center to its front.
- The mirror axis of rotation may not be normal to the ground plane;

The first of these factors results from the mirror axis of rotation being not normal to the CCD plane. We will remain in the same coordinate system and keep the assumptions that its origin is at the camera pinhole, and that the mirror axis of rotation is parallel to the ***Y*** axis.

The second of the misalignment factors, which results from a camera or CCD rotation in relation with the robot structure, can also be integrated as a rotation angle around the ***Y*** axis.

To generalize the solution for these two correction factors, we will start by performing a temporary shift of the coordinate system origin to point ***(0, -htf, 0)***. We will also assume a CCD center point translation offset given by (***-dx, 0, -dy***) and three rotation angles applied to the sensor: γ, ρ and θ, around the ***Y′***, ***X′*** and ***Z′*** axis respectively (Fig. 9).

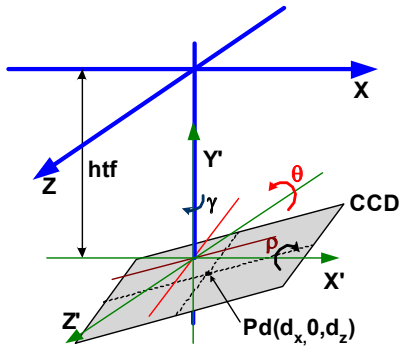

Fig. 9. New temporary coordinate system [***X′,Y′,Z′***] with origin at point (***0, -htf, 0***). ***γ***, ***ρ*** and ***θ***, are rotation angles around the ***Y′***, ***X′*** and ***Z′*** axis. ***Pd*** is the new offset CCD center.

These four geometrical transformations upon the original ***Pp*** pixel point can be obtained from the composition of the four homogeneous transformation matrices, resulting from their product

$$R_x(\rho)\bullet R_y(\gamma)\bullet R_z(\theta)\bullet T=\begin{bmatrix} t1_{\rho\gamma\theta} & t2_{\rho\gamma\theta} & t3_{\rho\gamma} & d_x \\ t1_{\rho\theta} & t2_{\rho\theta} & t3_{\rho} & 0 \\ t1_{\rho\gamma\theta} & t2_{\rho\gamma\theta} & t3_{\rho\gamma} & d_z \\ 0 & 0 & 0 & 1 \end{bmatrix} \tag{25}$$

The new start point ***Pp′(p′cx, p′cy, p′cz)***, already translated to the original coordinate system, can therefore be obtained from the following three equations:

$$p'_{cx}=p_{cx}(\cos(\gamma)\cos(\theta)+\sin(\rho)\sin(\gamma)\sin(\theta))+p_{cz}(\sin(\gamma)\cos(\rho))+d_x \tag{26}$$

$$p'_{cy}=p_{cx}(\cos(\rho)\sin(\theta)+p_{cz}\sin(\rho)-htf \tag{27}$$

$$p'_{cz}=p_{cx}(-\sin(\gamma)\cos(\theta)+\sin(\rho)\cos(\gamma)\sin(\theta))+p_{cz}(\cos(\gamma)\cos(\rho))+d_z \tag{28}$$

Analysis of the remaining problem can now follow from (5) substituting ***Pp′*** for ***Pp***.
Finally we can also deal with the third misalignment – resulting from the mirror axis of revolution not being normal to the ground – pretty much in the same way. We just have to temporarily shift the coordinate system origin to the point (***0, mtf-hmf, 0***), assume the original floor plane equation defined by its normal vector ***j*** and perform a similar geometrical transformation to this vector. This time, however, only rotation angles ***ρ*** and ***θ*** need to be applied. The new unit vector ***g***, will result as

$$g_{cx}=-\sin(\theta) \tag{29}$$

$$g_{cy}=\cos(\rho)\cos(\theta)-mtf+hmf \tag{30}$$

$$g_{cz}=\sin(\rho)\cos(\theta) \tag{31}$$

The rotated ground plane can therefore be expressed in Cartesian form as

$$g_{cx}X + g_{cy}Y + g_{cz}Z = g_{cy}(mtf - hmf) \tag{32}$$

Replacing the ***rt*** line equation (23) for the ***X***, ***Y*** and ***Z*** variables into (32), the intersection point can be found as a function of ***u***. Note that we still have to check if ***rt*** is parallel to the ground plane – which can be done by means of the ***rt*** and ***g*** dot product. This cartesian product can also be used to check if the angle between ***rt*** and ***g*** is obtuse, in which case the reflected ray will be above the horizon line.

4.3 Obtaining the model parameters

A method for fully automatic calculation of the model parameters, based only on the image of the soccer field, is still under development, with very promising results. Currently, most of the parameters can either be obtained automatically from the acquired image or measured directly from the setup itself. This is the case of the ground plane rotation relative to the mirror base, the distance between the mirror apex and the ground plane and the diameter of the mirror base. The first two values do not need to be numerically very precise since final results are still constrained by spatial resolution at the sensor level. A 10mm precision in the mirror to ground distance, for instance, will held an error within 60% of resolution imprecision and less than 0.2% of the real measured distance for any point in the ground plane. A 1 degree precision in the measurement of the ground plane rotation relative to the mirror base provides similar results with an error less than 0.16% of the real measured distance for any point in the ground plane.

Other parameters can be extracted from algorithmic analysis of the image or from a mixed approach. Consider, for instance, the thin lens law

$$f = \frac{g}{1 + G/B} \ . \tag{33}$$

where ***f*** is the lens focal distance, ***g*** is the lens to focal plane distance and ***G/B*** is the magnification factor. ***G/B*** is readily available from the diameter of the mirror outer rim in the sensor image; ***f*** can be obtained from the procedure described in section 3, while the actual pixel size is also defined by the sensor manufacturers. Since the magnification factor is also the ratio of distances between the lens focus and both the focus plane and the sensor plane, the ***g*** value can also be easily obtained from the known size of the mirror base and the mirror diameter size on the image.

The main image features used in this automatic extraction are the mirror outer rim diameter - assumed to be a circle -, the center of the mirror image and the center of the lens image.

5. Support visual tools and results

A set of software tools that support the procedure of distance map calibration for the CAMBADA robots, have been developed by the team. Although the misalignment parameters can actually be obtained from a set of features in the acquired image, the resulting map can still present minor distortions. This is due to the fact that spatial

resolution on the mirror image greatly degrades with distance – around 2cm/pixel at 1m, 5cm/pixel at 3m and 25cm/pixel at 5m. Since parameter extraction depends on feature recognition on the image, degradation of resolution actually places a bound on feature extraction fidelity. Therefore, apart from the basic application that provides the automatic extraction of the relevant image features and parameters, and in order to allow further trimming of these parameters, two simple image feedback tools have also been developed.
The base application treats the acquired image from any selected frame of the video stream. It starts by determining the mirror outer rim in the image, which, as can be seen in Fig. 10 may not be completely shown or centered in the acquired image. This feature extraction is obtained by analyzing 6 independent octants of the circle, starting at the image center line, and followed by a radial analysis of both luminance and chrominance radial derivative. All detected points belonging to the rim are further validated by a space window segmentation based on the first iteration guess of the mirror center coordinates and radius value, therefore excluding outliers. The third iteration produces the final values for the rim diameter and center point.

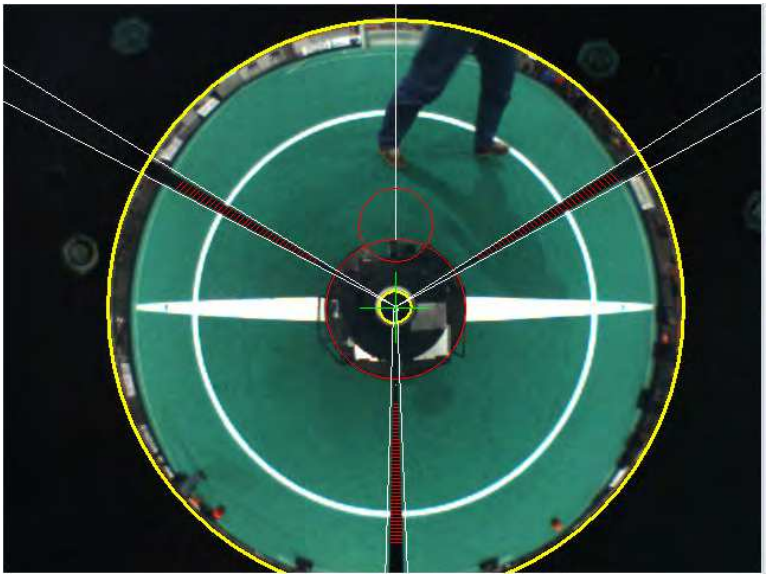

Fig. 10. Automatic extraction of main image features, while robot is standing at the center of a MSL middle field circle.

This first application also determines the lens center point in the image. To help this process, the lens outer body is painted white. Difference between mirror and lens center coordinates provides a first rough guess of the offset values between mirror axis and lens axis. This application also determines the robot body outer line and the robot heading, together with the limits, in the image, of the three vertical posts that support the mirror structure. These features are used for the generation of a mask image that invalidates all the pixels that are not relevant for real time image analysis.

Based on the parameters extracted from the first application and on those obtained from manufacturer data and from the correction procedure described in section 3, a second application calculates the pixel distance mapping on the ground plane, using the approach described in sections 4.1 and 4.2 (Fig. 11).

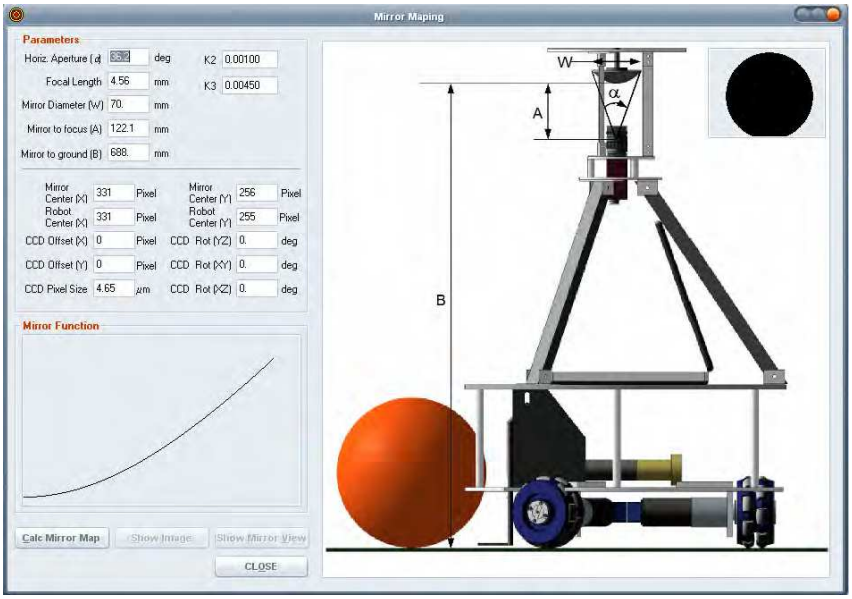

Fig. 11. Obtaining the pixel distance mapping on the ground plane; application interface.

All parameters can be manually corrected, if needed. The result is a matrix distance map, where each pixel coordinates serve as the line and column index and the distance values for each pixel are provided in both cartesian and polar coordinates referenced to the robot center. Since robot center and camera lens center may not be completely aligned, extraction of robot contour and center, performed by the first application, is also used to calculate the translation geometrical operation necessary to change the coordinate system origin from the center of the lens to the center of the robot.

Based on the generated distances maps, a third application constructs a bird's eye view of the omni-directional image, which is actually a reverse mapping of the acquired image into the real world distance map. The resulting image, depending on the zoom factor used, can result in a sparse image where, depending on the distance to the robot center, neighbor pixels in the CCD are actually several pixels apart in the resulting reconstruction. To increase legibility, empty pixels are filled with a luminance and chrominance value that is obtained by a weighted average of the values of the nearest four pixels as a function to the distance to each one of them. The result is a plane vision from above, allowing visual check of line parallelism and circular asymmetries (Fig. 12).

Finally, the last application generates a visual grid, with 0.5m distances between both lines and columns, which is superimposed on the original image. This provides an immediate visual clue for the need of possible further distance correction (Fig. 13).

Since the mid-field circle, used in this particular example setup, has exactly an outer diameter of 1m, incorrect distance map generation will be emphasized by grid and circle misalignment. This also provides a clear and simple visual clue of the parameters that need further correction, as well as the sign and direction of the needed correction.

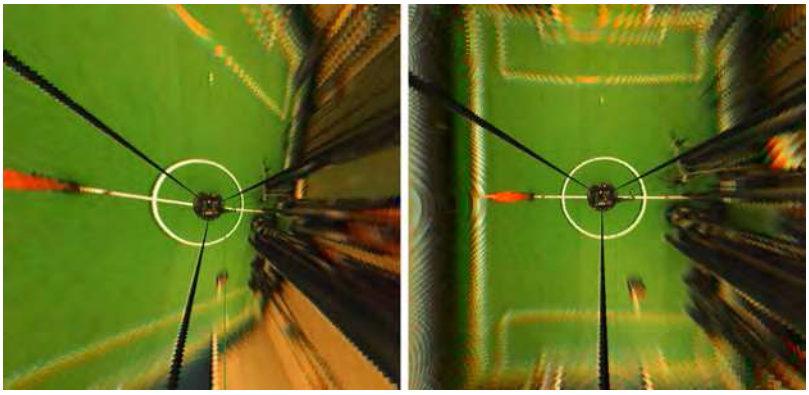

Fig. 12. Bird's eye view of the acquired image. On the left, the map was obtained with all misalignment parameters set to zero. On the right, after semi-automatic correction.

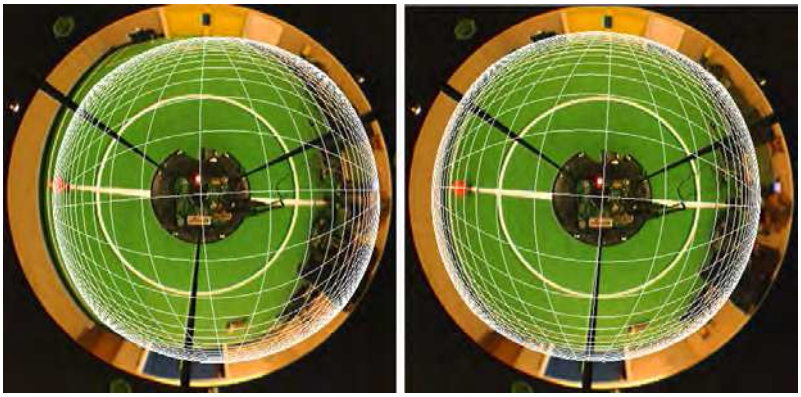

Fig. 13. A 0.5m grid, superimposed on the original image. On the left, with all correction parameters set to zero. On the right, the same grid after geometrical parameter extraction.

Furthermore, this tool provides on-line measurement feedback, both in cartesian and polar form, for any point in the image, by pointing at it with the mouse. Practical measurements performed at the team soccer field have shown really interesting results. Comparison between real distance values measured at more than 20 different field locations and the values taken from the generated map have shown errors always bellow twice the image spatial resolution. That is, the distance map has a precision that is better than +-1.5 cm at 1m, +-4cm at 2m and around +-20cm at 5m distances. These results are perfectly within the required bounds for the robot major tasks, namely object localization and self-localization on the field. The calibration procedure and map generation will take less than 5 seconds in full automatic mode, and normally less than one minute if further trimming is necessary.

6. Conclusions

Use of low cost cameras in a general-purpose omni-directional catadioptric vision system, without the aid of any precision adjustment mechanism, will normally preclude the use of a SVP approach. To overcome this limitation, this chapter explores a back propagation ray tracing geometrical algorithm ("*bird's eye view*") to obtain the ground plane distance map in the CAMBADA soccer robotic team. Taking into account the intrinsic combined spatial resolution of mirror and image sensor, the method provides viable and useful results that can actually be used in practical robotic applications. Although targeted at the Robocup MSL particular application, several other scenarios where mobile robots have to navigate in a non-structured or semi-structured environments can take advantage from this approach. This method is supported by a set of image analysis algorithms that can effectively extract the parameters needed to obtain a distance map with an error within the resolution bounds. Further trimming of these parameters can be manually and interactively performed, in case of need, with the support of a set of visual feedback tools that provide the user with an intuitive solution for analysis of the obtained results. This approach has proven to be very effective both from the spatial precision and time efficiency point of view. The CAMBADA team participates regularly in the Robocup International competition in the Middle Size League, where it ranked first in the 2008 edition, held in Suzhou, China, and third in the 2009 edition, held in Graz, Austria.

7. Acknowledgments

This work was partially supported by project ACORD, Adaptive Coordination of Robotic Teams, FCT/PTDC/EIA/70695/2006.

8. References

Aliaga, D. G., (2001), Accurate catadioptric calibration for realtime pose estimation of room-size environments, *Proceedings Of IEEE International Conference on Computer Vision*, pp. I: 127–134

Baker,S., Nayar, S. K. (1999). A theory of single-viewpoint catadioptric image formation. *International Journal of Computer Vision,* Volume 35, no. 2, pp 175–196.

Barreto, J. P. and Araujo, H. (2002), Geometric Properties of Central Catadioptric Line Images, *Proceedings of European Conference on Computer Vision*, Volume 4, pp. 237–251

Benosman,R., Kang., S.B. (Eds.) (2001). *Panoramic Vision - Sensors, Theory, and Applications*, Springer, ISBN: 978-0-387-95111-9

Blinn,J.F. (1977). A Homogeneous Formulation for Lines in 3D Space, *ACM SIGGRAPH Computer Graphics* , Volume 11, Issue 2, pp 237-241, ISSN:0097-8930

E. Menegatti F. Nori E. Pagello C. Pellizzari D. Spagnoli. (2001). Designing an omnidirectional vision system for a goalkeeper robot, In: *RoboCup-2001: Robot Soccer World Cup V*, A. Birk S. Coradeschi and P. Lima, (Ed.), pp 78–87, Springer, LNAI, 2377 , ISBN-13: 978-3540439127

Fabrizio, J. , Torel, J. and BenosmanR. (2002), Calibration of Panoramic Catadioptric Sensors made Easier, *Proceedings Of the Third Workshop on Omnidirectional Vision*, pp. 45–52

Foley, J.D., van Dam, A., Feiner,S.K., Hughes,J.F. (1995). *Computer Graphics: Principles and Practice in C*, Addison-Wesley Professional; 2 edition, ISBN-10: 0201848406

Geyer, C. and Daniilidis, K. , (2002), Paracatadioptric camera calibration. *IEEE Transations on Pattern Analysis and Machine Intelligence*, Volume 24, 5, pp. 687–695

Hartley, R., Zisserman, A. (2004). *Multiple View Geometry in Computer Vision*. Cambridge University Press, Second Edition, ISBN: 0521540518

Juergen Wolf (2003). Omnidirectional vision system for mobile robot localization in the Robocup environment, In: *Master's thesis*, Graz, University of Technology.

Kang, S. B. (2000), Catadioptric self-calibration, *Proceedings of IEEE Conference on Computer Vision and Pattern Recognition*, Volume 1, pp. 201–207

Lima, P., Bonarini1,A., Machado,C., Marchese1,F., Marques,C., Ribeiro,F., Sorrenti1,D. (2001). Omni-directional catadioptric vision for soccer robots. *Robotics and Autonomous Systems*, Volume 36, Issues 2-3 , 31, pp 87-102.

Mashita, T., Iwai, Y., Yachida. M. (2006), Calibration Method for Misaligned Catadioptric Camera, *IEICE - Transactions on Information and Systems archive,* Volume E89-D , Issue 7, pp. 1984-1993, ISSN:0916-8532

Menegatti, E. Pretto, A. Pagello, E. (2004). Testing omnidirectional vision-based Monte Carlo localization under occlusion, *Proceedings of the IEEE/RSJ Int. Conference on Intelligent Robots and Systems*, Volume 3, pp 2487- 2494

Micusik, B. and Pajdla, T. (2004), Para-catadioptric camera autocalibration from epipolar geometry, *Proceedings of Asian Conferenceon Computer Vision*, Volume 2, pp. 748–753

Micusik, B. and Pajdla, T. (2004), Autocalibration & 3D Reconstruction with Non-central Catadioptric Cameras, *Proceedings of IEEE Conference on Computer Vision and Pattern Recognition,* Volume 1, pp. 58–65

Micusik, B. and Pajdla, T. (2006), Para-catadioptric Camera Auto-Calibration from Epipolar Geometry, *IEICE - Transactions on Information and Systems archive*, Vol. E89-D , Issue 7, pp. 1984-1993, ISSN:0916-8532

Scaramussas, D., (2008), Omnidirectional Vision: From Calibration to Robot Motion Estimation, *Phd Thesis*, Roland Siegwart (ETH Zurich, thesis director), Università di Perugia, Italy

Stelow, D., Mishler, J., Koes, D. and Singh, S. (2001), Precise omnidirectional camera calibration, *Proceedings of IEEE Conference on Computer Vision and Pattern Recognition*, Volume 1, pp. 689–694

Voigtländer, A., Lange, S. , Lauer, M. and Riedmiller, M. (2007), Real-time 3D Ball Recognition using Perspective and Catadioptric Cameras, *Online Proceedings of the 3rd European Conference on Mobile Robots (ECMR)*

Ying, X. and Hu, Z. (2003), Catadioptric Camera Calibration Using Geometric Invariants, *Proceedings of IEEE International Conference on Computer Vision*, pp. 1351–1358

Zhang, Z. (2000), A Flexible New Technique for Camera Calibration. *IEEE Transactions on Pattern Analysis and Machine Intelligence*, vol. 22, no. 11, pp. 1330-1334, ISSN:0162-8828

Zivkovic, Z., Booij, O. (2006). How did we built our hyperbolic mirror omni-directional camera - practical issues and basic geometry, In: *IAS technical report IAS-UVA-05-04*, Intelligent Systems Laboratory Amsterdam, University of Amsterdam

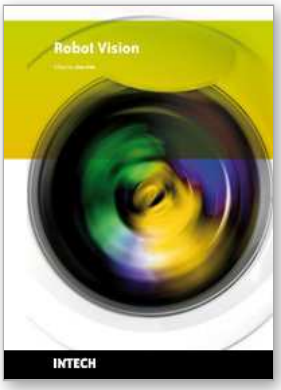

Robot Vision

Edited by Ales Ude

ISBN 978-953-307-077-3
Hard cover, 614 pages
Publisher InTech
Published online 01, March, 2010
Published in print edition March, 2010

The purpose of robot vision is to enable robots to perceive the external world in order to perform a large range of tasks such as navigation, visual servoing for object tracking and manipulation, object recognition and categorization, surveillance, and higher-level decision-making. Among different perceptual modalities, vision is arguably the most important one. It is therefore an essential building block of a cognitive robot. This book presents a snapshot of the wide variety of work in robot vision that is currently going on in different parts of the world.

InTech Europe
University Campus STeP Ri
Slavka Krautzeka 83/A
51000 Rijeka, Croatia
Phone: +385 (51) 770 447
Fax: +385 (51) 686 166
www.intechopen.com

InTech China
Unit 405, Office Block, Hotel Equatorial Shanghai
No.65, Yan An Road (West), Shanghai, 200040, China
中国上海市延安西路65号上海国际贵都大饭店办公楼405单元
Phone: +86-21-62489820
Fax: +86-21-62489821